Environmental Research Letters

PAPER

Satellite and airborne remote sensing of gross primary productivity in boreal Alaskan lakes

Catherine Kuhn[1], Matthew Bogard[1], Sarah Ellen Johnston[2], Aji John[3], Eric Vermote[4], Rob Spencer[2], Mark Dornblaser[5], Kim Wickland[5], Rob Striegl[5] and David Butman[1,6]

[1] Department of Forestry and Environmental Science, University of Washington, 4000 15th Avenue NE, Seattle, WA 98195-2100, United States of America
[2] Florida State University, Tallahassee, United States of America
[3] Department of Biology, University of Washington, Seattle, Washington, United States of America
[4] NASA Goddard Space Flight Center, GSFC Code 619, Greenbelt, MD 20771, United States of America
[5] U.S. Geological Survey, Boulder, United States of America
[6] Department of Civil and Environmental Engineering, University of Washington, Seattle, Washington, United States of America

E-mail: ckuhn@uw.edu

Keywords: freshwater ecosystems, Google Earth Engine, boreal, gross primary productivity, Landsat-8, Sentinel-2, lake color, remote sensing, shallow lakes

Supplementary material for this article is available online

OPEN ACCESS

RECEIVED
8 November 2019

REVISED
11 May 2020

ACCEPTED FOR PUBLICATION
9 July 2020

PUBLISHED
18 September 2020

Abstract

In terrestrial and marine ecosystems, remote sensing has been used to estimate gross primary productivity (GPP) for decades, but few applications exist for shallow freshwater ecosystems.Here we show field-based GPP correlates with satellite and airborne lake color across a range of optically and limnologically diverse lakes in interior Alaska. A strong relationship between *in situ* GPP derived from stable oxygen isotopes ($\delta^{18}O$) and space-based lake color from satellites (e.g. Landsat-8, Sentinel-2 and CubeSats) and airborne imagery (AVIRIS-NG) demonstrates the potential power of this technique for improving spatial and temporal monitoring of lake GPP when coupled with additional field validation measurements across different systems. In shallow waters clear enough for sunlight to reach lake bottoms, both submerged vegetation (macrophytes and algae) and phytoplankton likely contribute to GPP. The stable isotopes and remotely sensed shallow lake color used here integrate both components. These results demonstrate the utility of lake color as a feasible means for mapping lake GPP from remote sensing. This novel methodology estimates GPP from remote sensing in shallow lakes by combining field measurements of oxygen isotopes with airborne, satellite and CubeSat imagery. This use of lake color for providing insight into ecological processes of shallow lakes is recommended, especially for remote arctic and boreal landscapes.

1. Introduction

Northern high latitudes are warming at twice the global average rate (Overland *et al* 2019), driving widespread changes to terrestrial ecosystem structure and function (Pastick *et al* 2019, Wang *et al* 2019), including to gross primary productivity (GPP) (Myneni *et al* 1997, Goetz *et al* 2005, Beck and Goetz 2011). GPP is the rate primary producers convert inorganic carbon to biomass via photosynthetic pathways. Quantifying GPP can provide crucial insights into ecosystem functioning by establishing rates of food web carbon (C) uptake and energy flows.

Satellite remote sensing is a means to observe freshwater ecosystems at global scales. Satellite indices for productivity have been well-established for terrestrial (Tucker 1979, Pettorelli *et al* 2005) and marine (Antoine *et al* 1996, Lee *et al* 2015) systems from the red and near-infrared bands. While inland water remote sensing research has accelerated (Matthews 2011, Palmer *et al* 2015, Dörnhöfer and Oppelt 2016, Mouw *et al* 2017, Topp *et al* 2020), a comprehensive approach to efficiently map the spatial distribution of GPP for shallow lakes, which are globally abundant and concentrated in high northern latitudes (Downing *et al* 2006), has yet to emerge.

Past lake productivity studies used an approach adopted from oceanography that assumes phytoplankton drive GPP. Indices based on blue and green reflectance (Morel and Prieur 1977) are calculated to estimate phytoplankton biomass, which then drives net primary productivity models (Behrenfeld *et al* 2005, Shuchman *et al* 2013). Studies have primarily been limited to large water bodies (Bergamino *et al* 2010, Shuchman *et al* 2013, Yousef *et al* 2014, Kauer *et al* 2015, Fahnenstiel *et al* 2016, Deng *et al* 2017) and the method has even been applied for large (>1 km) lakes worldwide (Sayers *et al* 2015). However, this model relies on the assumption that there is no influence from bottom-reflectance (i.e. that lakes are optically deep).

However, worldwide 99% of all lakes are small (Downing *et al* 2006, Verpoorter *et al* 2014) and average lake depth globally has been estimated to only be 3.9 m (Messager *et al* 2016).

For these globally abundant small (<1 km) and shallow lakes (<10 m), the current method neglects benthic and littoral contributions to GPP from macrophytes and attached algae. Incorporating both benthic and pelagic processes into lake GPP models is crucial because macrophyte GPP rates exceed all other ecological communities including phytoplankton (Wetzel 2001) and can contribute 65%–98% of ecosystem production in shallow lakes (Jeppesen *et al* 1998, Rautio and Vincent 2006).

A remote sensing method for mapping GPP is needed that can integrate phytoplankton and macrophytes. This is especially relevant for the shallow lakes that dominate northern latitudes because of their potential relevance to carbon cycling and aquatic food webs (Raymond *et al* 2013, Wik *et al* 2016, Stanley and Del Giorgio 2018). The majority of shallow water remote sensing studies have focused on deriving bathymetry and fractional cover of aquatic vegetation (Kutser *et al* 2020). New field-based methods have emerged that account for contributions from phytoplankton and macrophytes in lakes (Bogard *et al* 2017) but remote sensing techniques have not caught up despite repeated calls for consistent, global inland water quality products (Malthus *et al* 2012) and the increasing availability of high-resolution satellite imagery.

This study describes a new approach for quantifying shallow lake GPP using high-resolution (<10 m) remote sensing and field measurements. We combine field observations of GPP derived from oxygen isotopes with high-resolution satellite imagery to estimate shallow lake GPP. We then assess this approach using independently collected field data and test the model across platforms. We also measured *in situ* properties including turbidity and absorbance to rule out their influence on results. Linking bottom-up field measurements of lake properties with top-down remote sensing provides a novel method to link in-lake ecosystem processes with spatially explicit data to investigate ecosystem function across arctic and boreal lakes.

2. Data and methods

2.1. Study area and field campaign overview

The Yukon Flats Basin is an extensive, 33 000 km^2 complex of low-lying lakes and wetlands inside the Yukon River Basin (figure 1). Dry, cold and underlain by discontinuous permafrost (Minsley *et al* 2012, Rey *et al* 2019), the region's continental sub-arctic climate has an annual average temperature of ∼−3 °C (Chen *et al* 2014) with short, ice-free summers (April/May to September/October) (Gallant 1995). Over 30 000 lakes dot this semi-arid landscape (Heglund and Jones 2003). Despite abundant surface water, the area receives very little precipitation (250 mm) and lake water balances are dominated by evaporation (Anderson *et al* 2013, 2019). Lakes are on the whole shallow and macrophyte-rich; historical surveys demonstrated that lake bottoms are carpeted with up to 80% coverage of aquatic vegetation (Glesne 1986).

Study lakes ($n = 7$) representative of the region were carefully selected based on results from historical surveys (Heglund and Jones 2003, Halm and Guldager 2012, Halm and Griffith 2014) and a 2016 field study (Bogard *et al* 2019) to represent a gradient taking into consideration depth, pH, dissolved organic carbon (DOC) concentration, chlorophyll-*a* and chromophoric dissolved organic matter (CDOM) absorption (table S1).

Lakes were sampled by boat and/or floatplane (figures 1(a) and (b)) during a 2018 field campaign conducted as part of the National Aeronautics and Space Administration's (NASA's) Arctic-Boreal Vulnerability Experiment (ABoVE) for a suite of parameters (section 2.2, text s1).

2.2. Field and laboratory methods for lake GPP and color

Detailed chemical and optical measurements were collected from the center of each lake as well as *in situ* surface reflectance (R_s). Lake GPP was estimated using an oxygen isotope ($\delta^{18}O$) mass balance approach adapted from (Quay *et al* 1995, Bocaniov *et al* 2012) as described in Bogard (2017) and text S1. For clarity, GPP derived from $\delta^{18}O$ field measurements will be referred to hereafter as *in situ* GPP in contrast to satellite-derived GPP. Turbidity, CDOM absorbance and phytoplankton chlorophyll-*a* were also measured to determine their influence, if any, on lake color. CDOM is the proportion of dissolved organic matter that absorbs strongly in ultraviolet and visible wavelengths (detailed methods in text S1).

2.3. Satellite observations of lake color

The launch of commercial small satellites with daily return times and the increasing availability of hyperspectral imagery through large-scale campaigns such

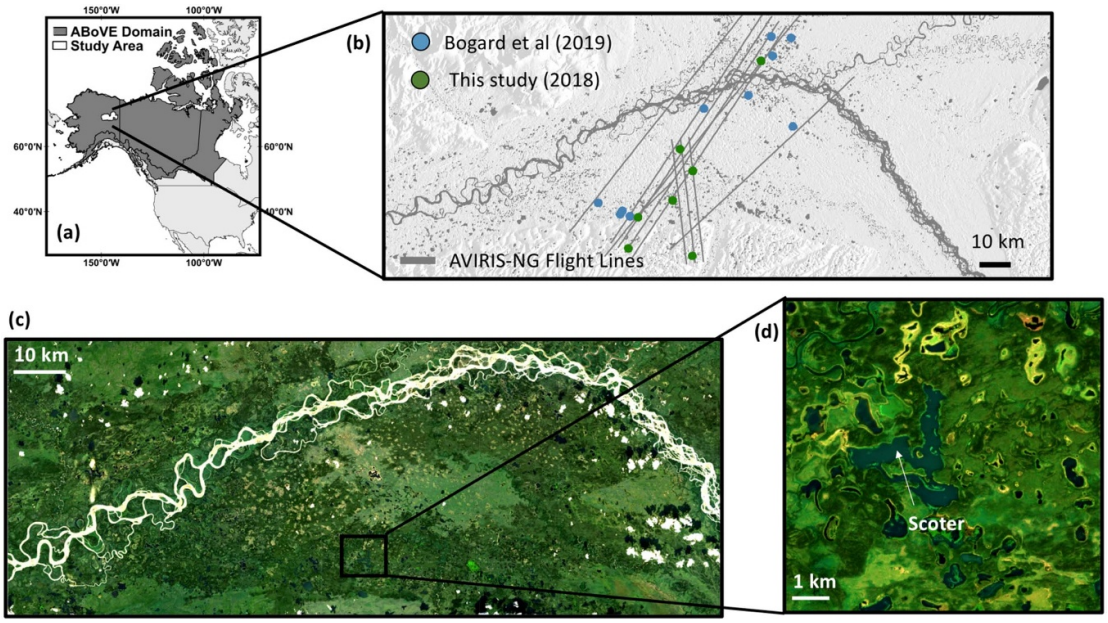

Figure 1. (a) Field site location in interior Alaska (b) Yukon Flats lakes sampled in 2016 ($n = 17$, in blue) and repeated in 2018 ($n = 7$, in green) field campaigns with AVIRIS-NG flight lines shown in grey (c) Yukon Flats landscape shown in natural color from Sentinel-2 tiles (table S2) collected on July 22, 2018 (d) Close-up of example study lake (Scoter) shown in Sentinel-2 natural color. The white arrow indicates where sample was collected on lake.

as NASA ABoVE has sparked interest in finer spatiotemporal analysis. In this study, we capitalize on the strengths of three different satellites: Landsat-8, Sentinel-2 and CubeSats (Planet, Inc). The sensors on-board Landsat-8 (L8), Sentinel-2 (S2) and PlanetScope (PS) all possess bands in the visible and near-infrared (VNIR) with varying spatial and temporal resolutions (figure 2). We also incorporate hyperspectral airborne imagery from AVIRIS-NG (figure 2).

As part of the ABoVE campaign, AVIRIS-NG imagery was acquired on July 22, 2018. Level-2 (L2) atmospherically corrected R_s (Bue *et al* 2015) was downloaded from https://avirisng.jpl.nasa.gov/dataportal/. Sentinel-2 acquisitions were identified and downloaded from the U.S. Geological Survey Earth Explorer (https://earthexplorer.usgs.gov/) and atmospherically corrected using the Land Surface Reflectance Code (LaSRC) (Vermote *et al* 2016). Sentinel-2 images were also corrected using the dark spectrum fitting (DSF) algorithm available in ACOLITE (Python Version 20 190 326.0), which is an open-source atmospheric correction tested successfully in coastal waters (Vanhellemont 2019). PlanetScope Level-2 products were identified using the Planet Labs API (Planet 2017) and a cloud-native, scalable workflow called SWEEP (John *et al* 2019). No cloud-free Landsat overpasses occurred during or close in time to field operations.

To utilize long-term Landsat records, we also calculated Landsat growing season composites, which is the per-pixel median greenness over the growing season (June, July and August). A common remote sensing tool used to quantify terrestrial productivity (Roy *et al* 2010), growing season composites provide a continuous, stable record of seasonal lake color. While Landsat overpasses are infrequent (16 d) compared to Planet (∼daily), the Landsat program has the longest global record of Earth observation with acquisitions initiated in the mid-1980s (Lymburner *et al* 2016), making it a powerful tool for historical analysis. For L8 composites, Collection 1 Level 2 R_s was accessed using Google Earth Engine. To generate seasonal composites, per-pixel median greenness was calculated from all cloud-free images acquired during the growing season (June 1–September 30) over the study area. With the exception of ACOLITE, all R_s products described above are derived using 6 SV-based approaches (Vermote *et al* 2006). For brevity only those results are shown in the main text, but ACOLITE results are given in figures S1–2 (available at stacks.iop.org/ERL/15/105001/mmedia), table S3.

2.4. In situ *surface reflectance validation data*

In order to verify *in situ* lake color, R_s (350–2500 nm) was measured at each lake center in 2018 ($n = 7$) using an ASD FieldSpec 4 High Resolution Spectroradiometer (3 nm and 8 nm resolution in VNIR and SWIR) (text S2). Above-water, *in situ* lake R_s was collected 3–5 d prior to overpasses because same-day *in situ* validation was not possible due to weather delays.

2.5. Combining field and satellite observations

Lake color was extracted for each sampling location from PlanetScope, Sentinel-2, Landsat-8 and AVIRIS scenes for each lake ($n = 7$) using Google Earth Engine (Gorelick *et al* 2017). A 3 × 3 pixel-wise box centered on field GPS coordinates was drawn for each

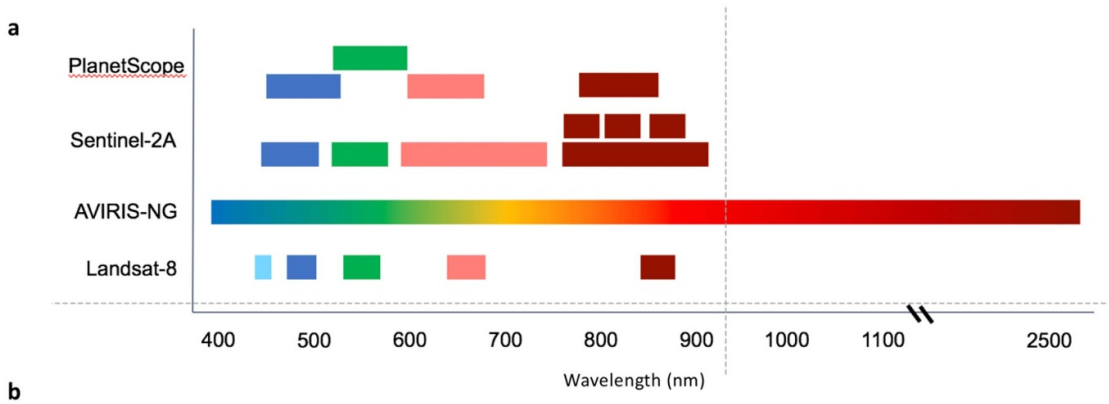

b

Craft	Sensor	Provider	Sensor Altitude (km)	Ground Sampling Distance
PlanetScope	CubeSat 3U	Planet Labs, Inc	475 km	3.0 m (approximate)
Sentinel-2 A/B	Multispectral Instrument (MSI)	European Space Agency (Europe)	786 km	10m (visible & near-infrared) 20m (shortwave infrared) 60m (atmospheric correction)
ERS-2	AVIRIS-NG	NASA Jet Propulsion Laboratory (JPL)	11km at high altitude, 1.9km at low altitude	4 to 20 m at altitude (4 to 20 km)
Landsat-8	Operational Land Imager (OLI)	National Aeronautics and Space Administration (NASA) (USA)	705 km	30m (visible & near-infrared) 15m (panchromatic & cirrus)

Figure 2. (a) Bandpass wavelengths (nm) in the visible bands and near-infrared for each sensor used in this study. The colors show the electromagnetic spectrum from blue (∼400 nm) to near-infrared (dark red, >700 nm). (b) Mission specifications for satellite and airborne imagery used in this study (b).

lake and the median R_s within each box was extracted from the image in order to reduce bias introduced by spatial sampling (Pahlevan *et al* 2016). In the case of scenes overlapping above a site, the median value between scenes was extracted. Since sampling was done at lake centers, all selected pixels were open water. A restrictive F-mask filter was also used to confirm selected pixels were water (Zhu *et al* 2015). Lake color from each respective platform was then regressed against *in situ* GPP ($n = 7$) using a reduced major axis (RMA) type II regression (Python package plyr2, (Haëntjens 2018)). This same workflow was also used to extract lake color from Landsat seasonal composites (section 2.3) for the 2016 samples ($n = 24$). The regression model was used to create satellite-derived maps of GPP by taking the regression equation derived from the GPP ∼ greenness relationship observed in the 2018 field campaign and applying it on a per-pixel basis to Sentinel-2 imagery using the green band as the model input.

2.6. Comparing surface reflectance across sensors

In order to make hyperspectral lake color comparable to multi-spectral observations, *in situ* and AVIRIS-NG R_s was spectrally convolved to Sentinel-2 wavelengths as in (Pahlevan *et al* 2017):

$$R_{rs}\left(\lambda_j\right) = \frac{\sum_{i=1}^{n} R_{rs}\left(\lambda_i\right) XRSR\left(\lambda_i\right)}{\sum_{i=1}^{n} R_{rs}\left(\lambda_i\right)}$$

where:

$R_{rs}\left(\lambda_j\right)$: band center wavelength

RSR: spectral response factor

n: total number of hyperspectral band centers (i)

Median absolute percent different (MAPD) was used to compare sensor R_s:

$$MAPD = median\left(abs\left(\frac{x-y}{x}\right)\right) * 100$$

where x is sensor 1 and y is sensor 2. For decadal time series analysis (figure 4), the non-parametric Mann–Kendall estimator and Sen's Slope were used to determine whether there was a positive or negative trend in lake greenness and its significance. Thiel–Sen Slope was calculated using the Scipy Python-based scientific computing package (Virtanen *et al* 2020) and significance of the slope was determined using a Mann–Kendall test (Hirsch *et al* 1982).

3. Results and discussion

3.1. In situ *lake GPP*

In situ median GPP rates (table 2) were high at 9.72 mg O_2 m^{-2} d^{-1} and spanned a wide range (interquartile range = 6.25 to 10.50 mg O_2 m^{-2} d^{-1}). *In situ* GPP is on the same order of magnitude as other free-water techniques estimating GPP (Solomon *et al* 2013). The rates observed here are higher than more dilute and often deeper boreal lakes (Ask *et al* 2012, Deininger *et al* 2017) and are consistent with the high productivity observed in shallow, macrophyte-rich lakes found in the northwestern Siberia lowlands (Manasypov *et al* 2014) and shallow lakes in the Mackenzie Delta (Squires *et al* 2009, Tank *et al* 2009).

Table 1. Sampling dates, coordinates and physical properties of study lakes sampled *in situ* in July 2018 for GPP, reflectance, dissolved organic matter composition and chlorophyll-*a* among others (section 2.2, text s1).

	Latitude	Longitude	Date Sampled	Depth (m)	Surface Area (km^2)
Boot (B)	66.07404	146.27066	7/18/18	22.0	0.73
Canvasback (CB)	66.38303	146.35489	7/19/18	1.4	2.83
Greenpepper (GP)	66.09209	146.73557	7/18/18	10.3	0.97
Ninemile (NM)	66.18285	146.66376	7/17/18	1.8	3.33
Scoter (SC)	66.24241	146.39896	7/17/18	4.5	4.56
YF17 (Y17)	66.32072	146.27431	7/17/18	1.6	1.75
YF20 (Y20)	66.63715	145.77278	7/17/18	1.3	0.59

Table 2. Limnological conditions for Yukon Flats sites sampled in 2018. Values given represent the means and, when more than two replicates were collected, standard deviations of the replicates are given as well.

	pH	Turbidity (FNU)	Chl-*a* ($\mu g\,l^{-1}$)	GPP ($g\,O_2\,m^{-2}\,d^{-1}$)	a440 (m^{-1})	DOC ($mg\,l^{-1}$)
Boot (B)	8.31	0.54	2.7 ± 0.05	3.0	1.2 ± 0.12	19.2 ± 0.21
Canvasback (CB)	9.55	0.96	2.26 ± 0.01	10.7	2.41 ± 0.17	29.83 ± 0.22
Greenpepper (GP)	9.02	0.96	4.1 ± 0.04	6.2	0.42 ± 0.03	32.82 ± 0.40
Ninemile (NM)	9.46	<0	6.5 ± 0.00	9.7	1.09 ± 0.31	27.64 ± 0.07
Scoter (SC)	8.93	<0	7.1 ± 0.05	6.3	0.47 ± 0.20	19.46 ± 0.08
YF17 (Y17)	9.82	35	83.3 ± 0.33	14.6	2.42 ± 0.59	35.65 ± 0.54
YF20 (Y20)	10.24	<0	1.26 ± 0.4	10.3	1.09 ± 0.83	10.17 ± 0.14

3.2. Controls on lake color

Other influences on lake color must be ruled out in order to avoid applying this empirical method over-ambitiously. To this end, we characterized variables (table 2) known to influence lake color, including phytoplankton pigments, CDOM and turbidity (Aurin and Dierssen 2012). We observed relatively low phytoplankton biomass based on HPLC Chl-*a* pigment analysis (median = 3.4 m^{-1}, interquartile range = 2.4–5.9 $\mu g\,l^{-1}$) (table 1). Overall, this is consistent with a previous study of 129 Yukon Flats lakes (table S1) showing Chl-*a* was lower than expected based on nutrient availability (Heglund and Jones 2003). The relatively clear waters and high GPP observed here in the presence of low phytoplankton biomass suggest macrophyte production is driving lake GPP (Genkai-Kato *et al* 2012). One exception was YF17, where field observations of a bloom were confirmed by high HPLC-derived Chl-*a* (83.3 $\mu g\,l^{-1}$)

The majority of lakes were shallow (median depth of 1.6 m) (table 1), with light extending to epiphytic periphyton and aquatic macrophytes. One lake was >10 m deep; the depth, low GPP and low Chl-*a* (table 2) of this lake provided an end-point representative of the gradient in the area. Other studies have established that submerged and floating macrophytes reflect in the green (560 nm) and near-infrared (850–880 nm) (Silva *et al* 2008, Oyama *et al* 2015, Palmer *et al* 2015, Dogliotti *et al* 2018). The shallow depths of these relatively clear lakes, as inferred by low turbidities (<1 FNU in most cases) could allow signals from macrophytes and periphyton to reach the surface (Mobley *et al* 2020). Given the low Chl-*a*, low turbidities and the observed presence of macrophytes within the water column we suggest that overall, phytoplankton production is not a significant component of the optical signature.

A second influence on lake color is absorption of light by CDOM. CDOM can interfere with the remote sensing of GPP in two ways. CDOM absorbs green light, so high CDOM has the direct effect of masking green light reflected from photosynthetic pigments (Carder *et al* 1989). Indirectly, CDOM can shade out aquatic producers, thus having the ecological impact of reducing GPP (Ask *et al* 2012, Seekell *et al* 2015). In order to rule out this influence, CDOM data were collected at each site. CDOM values (table 2) in sampled lakes were low (a_{440}, median = 1.13 m^{-1}, interquartile range = 0.78–1.82 m^{-1}), showing that lakes are relatively clear despite their high DOC (10.2 to 25.6 mg l^{-1}) (table 2). Our findings are consistent with other studies in semi-arid aquatic ecosystems (Osburn *et al* 2011, Bogard *et al* 2019, Kellerman *et al* 2019) that show low CDOM despite high DOC. While coupling between DOC and CDOM has been demonstrated at global scales (Massicotte *et al* 2017), CDOM-DOC decoupling in these semi-arid landscapes is hypothesized to result from decreased hydrologic connectivity which reduces terrestrial organic carbon subsidies as aromatic carbon compounds to aquatic ecosystems, resulting in clearer lakes than otherwise expected (Johnston *et al* 2020).

Finally, lake color can be influenced by scattering from sediment during periods of hydrologic connectivity to surface waters or during lake turnover. However, turbidity across lakes was low (<1 FNU) (table 2) with the exception of YF17, where the previously noted algal bloom drove turbidity up to 35 FNU. Taken together, these results indicate the

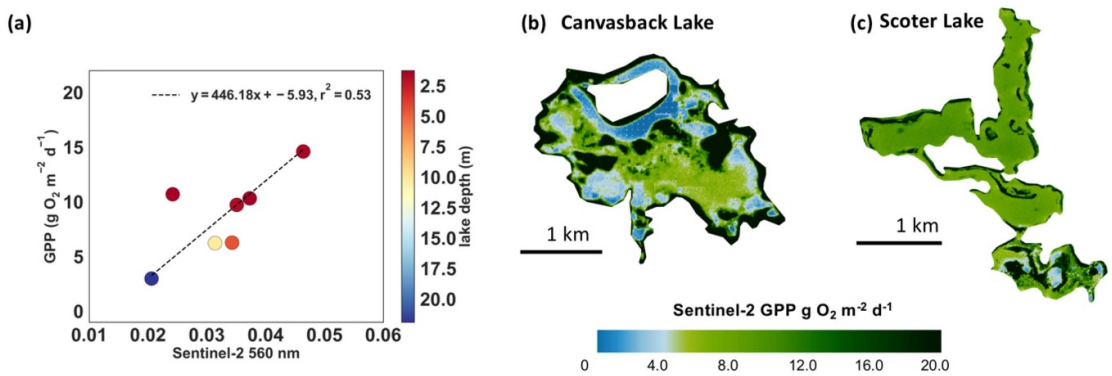

Figure 3. (a) Scatterplot showing the relationship between GPP measured *in situ* in 2018 and greenness as derived from Sentinel-2 surface reflectance (~560 nm) for July 2018 lake samples ($n = 7$). The equation shown in figure 3(a) was then applied per pixel to the Sentinel-2 imagery, resulting in spatially-explicit maps of GPP. Examples of these resulting GPP maps modeled from satellite imagery are shown for two of the study lakes: (b) Canvasback Lake and (c) Scoter Lake. The color bar indicates the range of values for modeled GPP derived by applying the equation in figure 3(a) to each Sentinel-2 pixel.

clear and shallow nature of these macrophyte-rich lakes creates favorable conditions for the remote sensing of benthic properties.

3.3. *Linking* in situ *GPP to Sentinel-2 lake color*

Lake color from satellite and airborne sensors was regressed against 2018 *in situ* GPP (mg O_2 m^{-2} d^{-1}) ($n = 7$), revealing a strong, positive correlation between greenness and GPP (figure 3(a), p-value < 0.05). We then applied this regression pixel-wise to Sentinel-2 imagery to create spatially explicit GPP maps (figures 3(b) and (c)) for each lake. Modeled, S2 GPP ranged from 3.9 ± 1.14 mg O_2 m^{-2} d^{-1} in the deep, upland Boot Lake to 14.21 ± 6.42 mg O_2 m^{-2} d^{-1} in shallow, eutrophic YF17.

3.4. Independent evaluation with Landsat

The relationship was then evaluated using a separate dataset from a 2016 field campaign that had been withheld for independent testing (figure 4). As same-week images were not available, we instead regressed seasonal L8 composites against 2018 ($n = 7$) and 2016 *in situ* GPP ($n = 17$) (Bogard *et al* 2019). The correlation between greenness and *in situ* GPP was maintained across both models.

The L8 seasonal composites produced a slightly stronger relationship (type 2 major axis regression: $y = 385.81x - 0.45$; $r^2 = 0.69$; $p = 2.60 \times 10^{-4}$, $n = 24$) than the Sentinel-2 same-week model. This likely results from the smoothing of short-term variability from the composite and the relative stability of oxygen pools (Bogard *et al* 2017) in these shallow lakes on seasonal scales. The separate models provide an independent check against each other, further substantiating the robustness of this approach across sensors and years.

The use of Landsat allows us to tap into the powerful historical imagery available through the Landsat archive in order to detect decadal (Wang *et al* 2014, Lymburner *et al* 2016) and seasonal (Kallio *et al* 2008) trends in lake color. Lake greenness computed for Scoter Lake (figure 5) showed a decline from 1984 to 2018. Field studies suggest that declines in greenness could result from increased CDOM absorption resulting from thermokarst processes for lakes with higher absorption (Wauthy *et al* 2018), increases in depth (Duguay and Lafleur 2003), or increased sediment loading during periods of surface water connectivity (Vonk *et al* 2015). Subsequent research combining these techniques with paleolimnology (Pienitz *et al* 1999, Bouchard *et al* 2017) and radiocarbon (Rühland *et al* 2003) data has the potential to unveil past lake processes, although more testing is required to establish mechanistic links between these processes and lake color across more diverse ecosystems.

3.5. *AVIRIS-NG, PlanetScope and* in situ R_s

Surface reflectance from different sensors showed the greatest agreement in the green band.

Using high-resolution PlanetScope and AVIRIS-NG R_s (table S2), Sentinel-2 and *in situ* R_s (figures 6, S1-2), we compared R_s and respective model performance using 2018 *in situ* GPP. Analyzing agreement between the blue, green, red and NIR bands, we found the best agreement in the green (MAPD median = 29%, interquartile range 8%–53%) (figure S1-2, text S3-4).

Green R_s is less subject to inter-sensor differences (Pahlevan *et al* 2018) and calibration errors between Landsat sensors (Vogelmann *et al* 2016). S2's green R_s has been successfully ground-truthed over small thermokarst lakes and ponds by Freitas *et al* (2019) and green R_s is also less impacted than NIR by particulates (Wang and Philpot 2007). Green R_s also has the major advantage of being measured by almost every spectral remote sensing platform, dating back to early Landsat (Dwyer *et al* 2018) and including the upcoming Plankton Aerosol, Cloud,

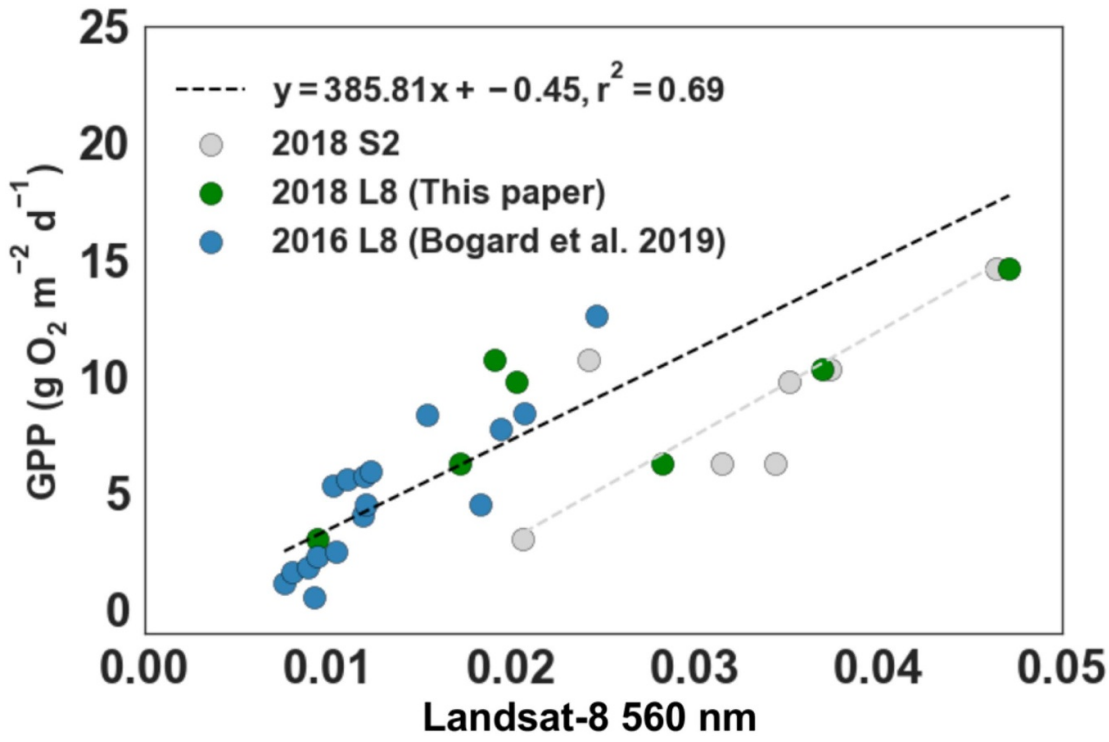

Figure 4. Scatter plot using L8 composites (R_s; 560 nm) and *in situ* GPP from 2016 and 2018 (g O_2 m^{-2} d^{-1}) ($n = 24$). The 2016 *in situ* GPP is the average of June and September; 2018 *in situ* GPP was collected once during July. The 2016 (shown in blue, $n = 17$) and 2018 (shown in green, $n = 7$) R_s was calculated from June to September composites (see text for full description). The S2 model from figure 1(d) ($n = 7$) is shown in grey for comparison. L8 regression model and coefficients of determination (r^2) are given in inset. Scene IDs can be found in table S2.

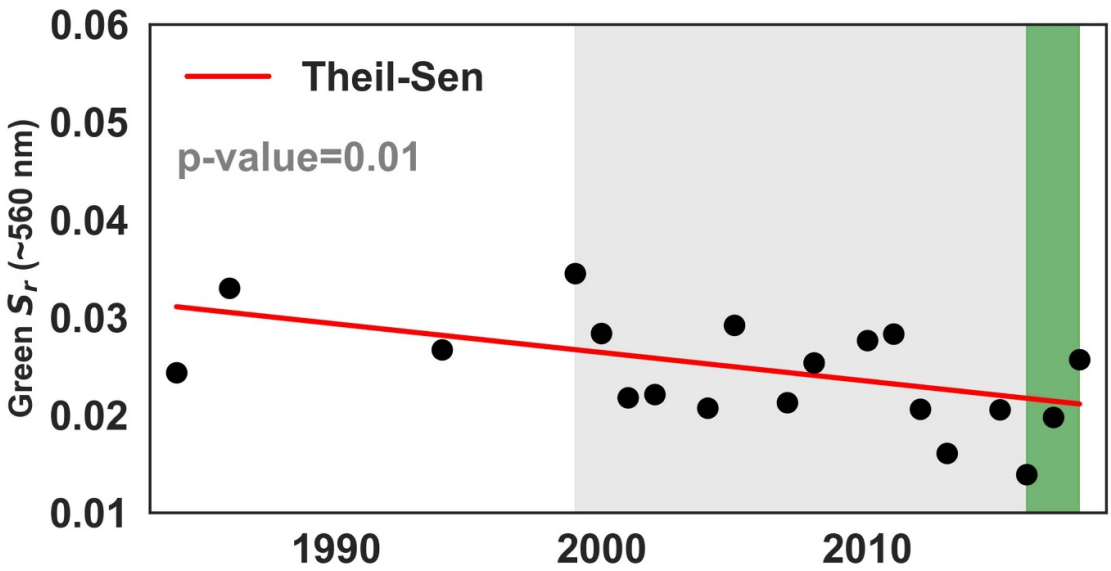

Figure 5. Landsat time series of greenness for Scoter Lake. Black dots represent median growing season greenness at the sampling location. The red line is the Thiel–Sen slope ($y = -0.00023x + 0.61$) with the p-value from the Mann–Kendall significance test given top left. Grey shading depicts launch of Landsat-7, after which two Landsat sensors have continuously been in orbit. Green shading represents time period of ABoVE field campaigns.

Ocean Ecosystem (PACE) Mission (Werdell *et al* 2019). Finally, previous studies have shown greenness covaries with both phytoplankton (O'Reilly *et al* 1998, O'Reilly and Werdell 2019) and macrophytes (Hestir *et al* 2015). In light of the larger disagreements between sensors detected in the NIR (text S4), these results suggest that green R_s may be a stable, sensor-agnostic quantity suitable for GPP modeling across a range of spectral, spatial and temporal resolutions.

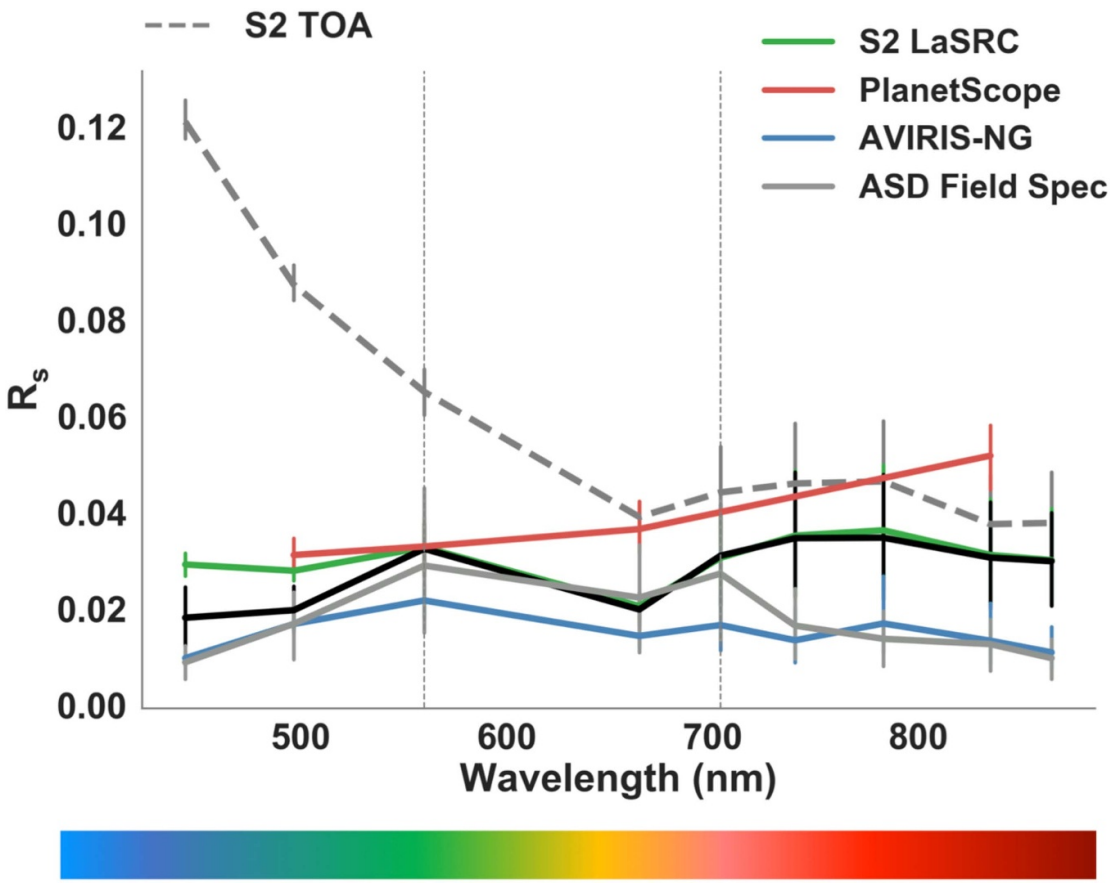

Figure 6. Surface reflectance (R_s) represented as the median and interquartile range (25%, 75%) of 2018 lakes. Dashed vertical grey lines show the wavelengths used to model GPP at 560 nm (green) and 704 nm (red-edge). S2 TOA spectra given for context. Extended discussion of differences given in text S3 and figure S2. It is important to note ASD measurements (table 1 for dates) were collected prior to airborne (July 22) and satellite (PlanetScope, July 23; Sentinel-2, July 22) measurements.

3.6. GPP model results for green and red-edge bands across sensors

In situ GPP (mg O_2 m^{-2} d^{-1}) corresponded with greenness (table 3, figures S3–4). The strongest correlation was between *in situ* GPP and *in situ* R_s ($r^2 = 0.68$; p-value < 0.05) and CubeSat R_s ($r^2 = 0.78$; p-value < 0.05). This could be due to two factors. First, *in situ* R_s was collected simultaneous to *in situ* GPP, in contrast to the overpasses 2–5 d later. However, unlike dynamic river and coastal systems, processes in these lakes vary on seasonal and annual scales. For example, high-frequency daily observations of dissolved oxygen collected from May to September (Bogard *et al* 2019) show consistently positive rates of net production driven by intense plant growth was sustained throughout most of the growing season. Johnston *et al* (2020) also showed diel dissolved organic matter composition and optical properties changed minimally over a 3 d period. A second reason for the stronger performance of PlanetScope and the *in situ* sensor's performance could be because of their finer spatial resolution relative to other sensors (10–30 m).

While restricting the time difference between field and satellite observations can improve model uncertainty in dynamic river systems (Kuhn *et al* 2019), albeit time differences of up to 3 to 5 d have been used successfully in several lake studies (Kloiber *et al* 2002, Chipman *et al* 2004, Olmanson *et al* 2008, Boucher *et al* 2018). Shorter time differences are ideal, yet given the temporal stability of the dissolved oxygen pool and water color over several days in these lakes, we are confident that these results are representative and provide important insights, particularly given the lack of comparisons of surface reflectance over inland waters (Maciel *et al* 2020).

A second advantage of Sentinel-2 over Landsat-8 is the addition of red-edge bands suitable for mapping vegetation. An even stronger correlation than with greenness was observed between GPP and the red-edge band (704 nm) (table 3, S3). Models improved by an average of 16% (table 3) due to the strong red-edge reflectance of macrophytes. This suggests that, when available, red-edge bands may be the strongest candidate for modeling GPP in these shallow lake ecosystems whose GPP is driven by both macrophytes and phytoplankton. This finding has implications for future missions as red-edge bands with narrower bandpasses are increasingly being added to, for example, Planet Lab's next-generation Dove satellites.

Table 3. Regression results between July 2018 R_s and *in situ* GPP fitted using a Type II regression model using the green (560 nm) and the red-edge (704 nm) bands from each sensor. The empty row results from PlanetScope lacking a red-edge band. All *p*-values were <0.05 (table S3) and individual scatterplots are provided in figures s3 and s4.

	Green (~560 nm)			Red-edge (~704 nm)		
	Slope	*Intercept*	r^2	*Slope*	*Intercept*	r^2
S2 TOA	478.91	−22.46	0.30	478.91	−22.46	0.56
S2 LaSRC	446.18	−5.93	0.53	446.18	−5.93	0.62
PlanetScope	413.39	−6.65	0.78	NA	NA	NA
AVIRIS-NG	607.19	−4.51	0.40	607.19	−4.51	0.74
ASD Field Spec	146.86	4.43	0.68	146.86	4.43	0.80

While the green band is suitable for historic analysis, these findings encourage red-edge based algorithm development due to the strong signal in these shallow arctic and boreal lakes.

The correlation between green and NIR bands with *in situ* GPP across sensors and sites indicates their potential as a simple GPP proxy for shallow lakes with low turbidity and CDOM. For context, global ocean models typically only explain 40% of water-column-integrated primary production (Siegel *et al* 2001). The strength of this relationship between lake color and *in situ* GPP for both 2016 and 2018 datasets suggests potential for the development of a remote sensing modeling framework for shallow lake GPP.

4. Conclusions

This study provides evidence of a simple empirical relationship between lake color and GPP for shallow, relatively clear boreal lakes using *in situ* field data paired with remote sensing. We use a novel approach that pairs oxygen isotopes with satellite imagery. Both techniques integrate pelagic and benthic processes from phytoplankton and macrophytes in shallow waters (Wetzel and Hough 1972, Jackson 2003). Summertime CO_2 drawdown in shallow lakes has been linked to macrophyte growth, highlighting the potentially important role of macrophytes in lake carbon cycling (Tank *et al* 2009, Vesterinen *et al* 2016). Shallow lakes are abundant worldwide and therefore the ability to integrate benthic and pelagic GPP is crucial for capturing whole ecosystem GPP.

In terrestrial systems, NDVI has been widely adopted as a useful, albeit imperfect, proxy for vegetation biomass (Rouse 1974). NDVI has transformed our understanding of landscape change in remote northern regions (Jia *et al* 2003, Goetz *et al* 2005, Bhatt *et al* 2013, Ju and Masek 2016, Sulla-Menashe *et al* 2018), yet no such metric has been adopted for shallow lakes. This study provides initial evidence of the green band as a potential simple index for mapping GPP in shallow, light-filled, and highly productive northern lakes. We then confirmed this relationship using Landsat-8 and compare results from other sensors including AVIRIS-NG and PlanetScope. This study demonstrates green and red-edge bands from Sentinel-2, Landsat-8, AVIRIS-NG and PlanetScope can be used to map GPP when constrained with appropriate field data. More detailed *in situ* measurements of lake color and biogeochemistry across optically diverse systems are needed to further test this finding. Advances in field data collection needs to be prioritized for algorithm development across the circumpolar north.

In the Yukon Flats, warming and thawing has led to lake area decline (Jepsen *et al* 2013, 2016). Surveying all 30 000 lakes in this region is not feasible yet the area is predicted to undergo drastic hydrologic changes linked to increasing permafrost thaw (Walvoord and Striegl 2007, Walvoord *et al* 2012). Our findings suggest further work developing remote sensing algorithms for GPP could advance lake monitoring at scales useful for climate science and ecosystem management.

Acknowledgments

This research was supported by a NASA Earth and Space Science Fellowship (NESSF) awarded to CDK. Data collection was also supported by NASA-ABoVE Project 14-14TE-0012 (awards NNH16AC03I and NNX15AU14A) and the U.S. Geological Survey (USGS) Land Carbon Program. Sample collection was made possible by the expert flights in and out of lakes by Jim Webster (Webster's Flying Service). We thank the Remote Sensing and Geospatial Analysis Laboratory (RSGAL) lab for the use of the ASD Field Spectrometer. Any use of trade, firm, or product names is for descriptive purposes only and does not imply endorsement by the U.S. Government. We also thank three anonymous reviewers for their constructive comments.

Data availability statement

Any data that support the findings of this study are included within the article.

ORCID iDs

Catherine Kuhn https://orcid.org/0000-0002-9220-630X

Matthew Bogard https://orcid.org/0000-0001-9491-0328
Sarah Ellen Johnston https://orcid.org/0000-0002-6237-0379
Aji John https://orcid.org/0000-0002-4401-1401
Rob Spencer https://orcid.org/0000-0003-0860-4717
Mark Dornblaser https://orcid.org/0000-0002-6298-3757
Kim Wickland https://orcid.org/0000-0002-6400-0590
Rob Striegl https://orcid.org/0000-0002-8251-4659
David Butman https://orcid.org/0000-0003-3520-7426

References

Anderson L, Birks J, Rover J and Guldager N 2013 Controls on recent Alaskan lake changes identified from water isotopes and remote sensing *Geophys. Res. Lett.* **40** 3413–8
Anderson L, Edwards M, Shapley M D, Finney B P and Langdon C 2019 Holocene thermokarst lake dynamics in northern Interior Alaska: the interplay of climate, fire, and subsurface hydrology *Front. Earth Sci.* **7**
Antoine D, André J and Morel A 1996 Oceanic primary production: 2. estimation at global scale from satellite (coastal zone color scanner) chlorophyll *Global Biogeochem. Cycles* **10** 57–69
Ask J, Karlsson J and Jansson M 2012 Net ecosystem production in clear-water and brown-water lakes *Global Biogeochem. Cycles* **26**
Aurin D A and Dierssen H M 2012 Advantages and limitations of ocean color remote sensing in CDOM-dominated, mineral-rich coastal and estuarine waters *Remote Sens. Environ.* **125** 181–97
Beck P S A and Goetz S J 2011 Satellite observations of high northern latitude vegetation productivity changes between 1982 and 2008: ecological variability and regional differences *Environ. Res. Lett.* **6** 45501
Behrenfeld M J, Boss E, Siegel D A and Shea D M 2005 Carbon-based ocean productivity and phytoplankton physiology from space *Global Biogeochem. Cycles* **19**
Bergamino N *et al* 2010 Spatio-temporal dynamics of phytoplankton and primary production in Lake Tanganyika using a MODIS based bio-optical time series *Remote Sens. Environ.* **114** 772–80
Bhatt U *et al* 2013 Recent declines in warming and vegetation greening trends over pan-Arctic Tundra *Remote Sens.* **5** 4229–54
Bocaniov S A, Schiff S L and Smith R E H 2012 Plankton metabolism and physical forcing in a productive embayment of a large oligotrophic lake: insights from stable oxygen isotopes *Freshwater Biol.* **57** 481–96
Bogard M J *et al* 2019 Negligible cycling of terrestrial carbon in many lakes of the arid circumpolar landscape *Nat. Geosci.* **12** 180–5
Bogard M J, Vachon D, St.-Gelais N F and Del Giorgio P A 2017 Using oxygen stable isotopes to quantify ecosystem metabolism in northern lakes *Biogeochemistry* **133** 347–64
Bouchard F *et al* 2017 Paleolimnology of thermokarst lakes: a window into permafrost landscape evolution *Arct. Sci.* **3** 91–117
Boucher J, Weathers K C, Norouzi H and Steele B 2018 Assessing the effectiveness of Landsat 8 chlorophyll a retrieval algorithms for regional freshwater monitoring *Ecol. Appl.* **28** 1044–54
Bue B D, Thompson D R, Eastwood M, Green R O, Gao B-C, Keymeulen D, Sarture C M, Mazer A S and Luong H H 2015 Real-time atmospheric correction of AVIRIS-NG imagery *IEEE Trans. Geosci. Remote Sens.* **53** 6419–28
Carder K L, Steward R G, Harvey G R and Ortner P B 1989 Marine humic and fulvic acids: their effects on remote sensing of ocean chlorophyll *Limnol. Oceanogr.* **34** 68–81
Chen M, Rowland J C, Wilson C J, Altmann G L and Brumby S P 2014 Temporal and spatial pattern of thermokarst lake area changes at Yukon Flats, Alaska *Hydrol. Processes* **28** 837–52
Chipman J W, Lillesand T M, Schmaltz J E, Leale J E and Nordheim M J 2004 Mapping lake water clarity with Landsat images in Wisconsin, USA *Can. J. Remote Sens.* **30** 1–7
Deininger A, Faithfull C L and Bergström A 2017 Phytoplankton response to whole lake inorganic N fertilization along a gradient in dissolved organic carbon *Ecology* **98** 982–94
Deng Y, Zhang Y, Li D, Shi K and Zhang Y 2017 Temporal and spatial dynamics of phytoplankton primary production in Lake Taihu derived from MODIS data *Remote Sens.* **9** 195
Dogliotti A, Gossn J, Vanhellemont Q and Ruddick K 2018 Detecting and quantifying a massive invasion of floating aquatic plants in the Río de la Plata turbid waters using high spatial resolution ocean color imagery *Remote Sens.* **10** 1140
Dörnhöfer K and Oppelt N 2016 Remote sensing for lake research and monitoring – recent advances *Ecol. Indic.* **64** 105–22
Downing J A *et al* 2006 The global abundance and size distribution of lakes, ponds, and impoundments *Limnol. Oceanogr.* **51** 2388–97
Duguay C R and Lafleur P M 2003 Determining depth and ice thickness of shallow sub-Arctic lakes using space-borne optical and SAR data *Int. J. Remote Sens.* **24** 475–89
Dwyer J *et al* 2018 Analysis ready data: enabling analysis of the Landsat Archive *Remote Sens.* **10** 1363
Fahnenstiel G L, Sayers M J, Shuchman R A, Yousef F and Pothoven S A 2016 Lake-wide phytoplankton production and abundance in the Upper Great Lakes: 2010–2013 *J. Great Lakes Res.* **42** 619–29
Freitas P, Vieira G, Canário J, Folhas D and Vincent W 2019 Identification of a threshold minimum area for reflectance retrieval from thermokarst lakes and ponds using full-pixel data from Sentinel-2 *Remote Sens.* **11** 657
Gallant A L 1995 *Ecoregions of Alaska* No. 1567 (Washington, DC: US Government Printing Office) (https://pubs.er.usgs.gov/publication/pp1567)
Genkai-Kato M, Vadeboncoeur Y, Liboriussen L and Jeppesen E 2012 Benthic–planktonic coupling, regime shifts, and whole-lake primary production in shallow lakes *Ecology* **93** 619–31
Glesne R S 1986 Lake fishery habitat survey and classification on interior Alaska National Wildlife Refuges, 1984 and 1985 *Report No. FY86–2* (Anchorage, AK: U.S. Fish and Wildlife Service, Fairbanks Fishery Resource Office)
Goetz S J, Bunn A G, Fiske G J and Houghton R A 2005 Satellite-observed photosynthetic trends across boreal North America associated with climate and fire disturbance *Proc. Natl Acad. Sci.* **102** 13521–5
Gorelick N, Hancher M, Dixon M, Ilyushchenko S, Thau D and Moore R 2017 google earth engine: planetary-scale geospatial analysis for everyone *Remote Sens. Environ.* **202** 18–27
Haëntjens N 2018 plyr2 0.1.0 PyPi. available at: https://pypi.org/project/pylr2/
Halm D R and Griffith B 2014 Water-quality Data from Lakes in the Yukon Flats, Alaska, 2010–2011 *USGS Open File Report 1181* (Reston, VA: US Geological Survey) (https://pubs.usgs.gov/of/2014/1181/)
Halm D R and Guldager N 2012 Water-quality Data of Lakes and Wetlands in the Yukon Flats, Alaska, 2007–2009 (Reston, VA: US Geological Survey)
Heglund P J and Jones J R 2003 Limnology of shallow lakes in the Yukon Flats National Wildlife Refuge, Interior Alaska *Lake Reservoir Manage.* **19** 133–40
Hestir E L *et al* 2015 Measuring freshwater aquatic ecosystems: the need for a hyperspectral global mapping satellite mission *Remote Sens. Environ.* **167** 181–95

Hirsch R M, Slack J R and Smith R A 1982 Techniques of trend analysis for monthly water quality data *Water Resour. Res.* **18** 107–21

Jackson L J 2003 Macrophyte-dominated and turbid states of shallow lakes: evidence from Alberta lakes *Ecosystems* **6** 213–23

Jeppesen E *et al* 1998 Impact of submerged macrophytes on fish-zooplankton interactions in lakes *The Structuring Role of Submerged Macrophytes in Lakes* (Berlin: Springer) pp 91–114

Jepsen S M, Voss C I, Walvoord M A, Rose J R, Minsley B J and Smith B D 2013 Sensitivity analysis of lake mass balance in discontinuous permafrost: the example of disappearing Twelvemile Lake, Yukon Flats, Alaska (USA) *Hydrogeol J.* **21** 185–200

Jepsen S M, Walvoord M A, Voss C I and Rover J 2016 Effect of permafrost thaw on the dynamics of lakes recharged by ice-jam floods: case study of Yukon Flats, Alaska *Hydrol. Processes* **30** 1782–95

Jia G J, Epstein H E and Walker D A 2003 Greening of arctic Alaska, 1981-2001 *Geophys. Res. Lett.* **30** 2067

John A *et al* 2019 SWEEP: accelerating scientific research through scalable serverless workflows *CC '19 Companion: IEEE/ACM 12th Int. Conf. on Utility and Cloud Computing Companion Proc.* (Auckland, New Zealand) available at: https://ucc-conference.org/

Johnston S E *et al* 2020 Hydrologic connectivity determines dissolved organic matter biogeochemistry in northern high-latitude lakes *Limnol. Oceanogr.* **65** 1764–80

Ju J and Masek J G 2016 The vegetation greenness trend in Canada and US Alaska from 1984–2012 Landsat data *Remote Sens. Environ.* **176** 1–16

Kallio K, Attila J, Härmä P, Koponen S, Pulliainen J, Hyytiäinen U-M and Pyhälahti T 2008 Landsat ETM+ images in the estimation of seasonal lake water quality in boreal river basins *Environ. Manage.* **42** 511–22

Kauer T, Kutser T, Arst H, Danckaert T and Nõges T 2015 Modelling primary production in shallow well mixed lakes based on MERIS satellite data *Remote Sens. Environ.* **163** 253–61

Kellerman A M *et al* 2019 'Fundamental drivers of dissolved organic matter composition across an Arctic effective precipitation gradient' *Limnol. Oceanogr.* **10** 1–18

Kloiber S M, Brezonik P L, Olmanson L G and Bauer M E 2002 A procedure for regional lake water clarity assessment using Landsat multispectral data *Remote Sens. Environ.* **82** 38–47

Kuhn C *et al* 2019 Performance of Landsat-8 and Sentinel-2 surface reflectance products for river remote sensing retrievals of chlorophyll-a and turbidity *Remote Sens. Environ.* **224** 104–18

Kutser T *et al* 2020 Remote sensing of shallow waters – A 50 year retrospective and future directions *Remote Sens. Environ.* **240** 111619

Lee Z, Marra J, Perry M J and Kahru M 2015 Estimating oceanic primary productivity from ocean color remote sensing: A strategic assessment *J. Mar. Syst.* **149** 50–59

Lymburner L, Botha E, Hestir E, Anstee J, Sagar S, Dekker A and Malthus T 2016 Landsat 8: providing continuity and increased precision for measuring multi-decadal time series of total suspended matter *Remote Sens. Environ.* **185** 108–18

Maciel D A, Novo E M L D M, Barbosa C C F, Martins V S, Flores Júnior R, Oliveira A H, Sander De Carvalho L A and Lobo F D L 2020 Evaluating the potential of CubeSats for remote sensing reflectance retrieval over inland waters *Int. J. Remote Sens.* **41** 2807–17

Malthus T J, Hestir E L, Dekker A G and Brando V E 2012 The case for a global inland water quality product *2012 IEEE Int. Geoscience and Remote Sensing Symp.* (Piscataway, NJ: IEEE) pp 5234–7

Manasypov R M, Pokrovsky O S, Kirpotin S N and Shirokova L S 2014 Thermokarst lake waters across the permafrost zones of western Siberia *Cryosphere* **8** 1177–93

Massicotte P, Asmala E, Stedmon C and Markager S 2017 Global distribution of dissolved organic matter along the aquatic continuum: across rivers, lakes and oceans *Sci.Total Environ.* **609** 180–191

Matthews M W 2011 A current review of empirical procedures of remote sensing in inland and near-coastal transitional waters *Int. J. Remote Sens.* **32** 6855–6899

Messager M L, Lehner B, Grill G, Nedeva I and Schmitt O 2016 Estimating the volume and age of water stored in global lakes using a geo-statistical approach *Nat. Commun.* **7** 13603

Minsley B J *et al* 2012 Airborne electromagnetic imaging of discontinuous permafrost *Geophys. Res. Lett.* **39** L02503

Mobley C, Boss E and Roesler C 2020 *NASA Ocean Optics Web Book* 2020th edn. Edited by N. grant NNX14AQ49G Creative Commons available at: https://oceanopticsbook.info/view/references/publications

Morel A and Prieur L 1977 Analysis of variations in ocean color&#x2019 *Limnol. Oceanogr.* **22** 709–22

Mouw C B *et al* 2017 A consumer's guide to satellite remote sensing of multiple phytoplankton groups in the global ocean *Front. Mar. Sci.* **4** 41

Myneni R B, Keeling C D, Tucker C J, Asrar G and Nemani R R 1997 Increased plant growth in the northern high latitudes from 1981 to 1991 *Nature* **386** 698

O'Reilly J E, Maritorena S, Mitchell B G, Siegel D A, Carder K L, Garver S A, Kahru M and Mcclain C 1998 Ocean color chlorophyll algorithms for SeaWiFS *J. Geophys. Res.* **103** 24937–53

O'Reilly J E and Werdell P J 2019 Chlorophyll algorithms for ocean color sensors-OC4, OC5 & OC6 *Remote Sens. Environ.* **229** 32–47

Olmanson L G, Bauer M E and Brezonik P L 2008 A 20-year Landsat water clarity census of Minnesota's 10,000 lakes *Remote Sens. Environ.* **112** 4086–97

Osburn C L, Wigdahl C R, Fritz S C and Saros J E 2011 Dissolved organic matter composition and photoreactivity in prairie lakes of the US Great Plains *Limnol. Oceanogr.* **56** 2371–90

Overland J E *et al* 2019 Ivory gull: status, trends and new knowledge Acrtic Report Card 2019 (Silver Spring, MD: NOAA)

Overland J E and Wang M 2005 The Arctic climate paradox: the recent decrease of the Arctic Oscillation *Geophys. Res. Lett.* **32**

Oyama Y, Matsushita B and Fukushima T 2015 Distinguishing surface cyanobacterial blooms and aquatic macrophytes using Landsat/TM and ETM+ shortwave infrared bands *Remote Sens. Environ.* **157** 35–47

Pahlevan N, Balasubramanian S, Sarkar S and Franz B 2018 Toward long-term Aquatic science products from heritage landsat missions *Remote Sens.* **10** 1337

Pahlevan N, Sarkar S and Franz B A 2016 Uncertainties in coastal ocean color products: impacts of spatial sampling *Remote Sens. Environ.* **181** 14–26

Pahlevan N, Smith B, Binding C and O'Donnell D M 2017 Spectral band adjustments for remote sensing reflectance spectra in coastal/inland waters *Opt. Express* **25** 28650–67

Palmer S C J, Kutser T and Hunter P D 2015 Remote sensing of inland waters: challenges, progress and future directions *Remote Sens. Environ.* **157** 1–8

Pastick N J, Jorgenson M T, Goetz S J, Jones B M, Wylie B K, Minsley B J, Genet H, Knight J F, Swanson D K and Jorgenson J C 2019 Spatiotemporal remote sensing of ecosystem change and causation across Alaska *Global Change Biol.* **25** 1171–89

Pettorelli N, Vik J O, Mysterud A, Gaillard J-M, Tucker C J and Stenseth N C 2005 Using the satellite-derived NDVI to assess ecological responses to environmental change *Trends Ecol. Evol.* **20** 503–10

Pienitz R, Smol J P and Macdonald G M 1999 Paleolimnological reconstruction of Holocene climatic trends from two boreal treeline lakes, Northwest Territories, Canada *Arct. Antarct. Alp. Res.* **31** 82–93

Planet 2017 Planet Application Program Interface: in Space for Life on Earth (San Francisco) available at: https://api.planet.com

Quay P D, Wilbur D, Richey J E, Devol A H, Benner R and Forsberg B R 1995 The 18O: 16O of dissolved oxygen in rivers and lakes in the Amazon Basin: determining the ratio of respiration to photosynthesis rates in freshwaters *Limnol. Oceanogr.* **40** 718–29

Rautio M and Vincent W F 2006 Benthic and pelagic food resources for zooplankton in shallow high-latitude lakes and ponds *Freshwater Biol.* **51** 1038–52

Raymond P A *et al* 2013 Global carbon dioxide emissions from inland waters *Nature* **503** 355–9

Rey D M, Walvoord M, Minsley B, Rover J and Singha K 2019 Investigating lake-area dynamics across a permafrost-thaw spectrum using airborne electromagnetic surveys and remote sensing time-series data in Yukon Flats, Alaska *Environ. Res. Lett.* **14** 25001

Rouse J W 1974 Monitoring the vernal advancement of retrogradation of natural vegetation, NASA/GSFG, Type III *Final Report 371* (https://ntrs.nasa.gov/citations/19730009608)

Roy D P, Ju J, Kline K, Scaramuzza P L, Kovalskyy V, Hansen M, Loveland T R, Vermote E and Zhang C 2010 Web-enabled Landsat Data (WELD): landsat ETM+ composited mosaics of the conterminous United States *Remote Sens. Environ.* **114** 35–49

Rühland K, Priesnitz A and Smol J P 2003 Paleolimnological evidence from diatoms for recent environmental changes in 50 lakes across Canadian Arctic treeline *Arct. Antarct. Alp. Res.* **35** 110–23

Sayers M J *et al* 2015 A new method to generate a high-resolution global distribution map of lake chlorophyll *Int. J. Remote Sens.* **36** 1942–64

Seekell D A *et al* 2015 The influence of dissolved organic carbon on primary production in northern lakes *Limnol. Oceanogr.* **60** 1276–85

Shuchman R A, Sayers M, Fahnenstiel G L and Leshkevich G 2013 A model for determining satellite-derived primary productivity estimates for Lake Michigan *J. Great Lakes Res.* **39** 46–54

Siegel D A *et al* 2001 Bio-optical modeling of primary production on regional scales: the Bermuda BioOptics project *Deep-Sea Res.* II **48** 1865–96

Silva T S F, Costa M P F, Melack J M and Novo E M L M 2008 Remote sensing of aquatic vegetation: theory and applications *Environ. Monit. Assess.* **140** 131–45

Solomon C T *et al* 2013 Ecosystem respiration: drivers of daily variability and background respiration in lakes around the globe *Limnol. Oceanogr.* **58** 849–66

Squires M M, Lesack L F W, Hecky R E, Guildford S J, Ramlal P and Higgins S N 2009 Primary production and carbon dioxide metabolic balance of a lake-rich arctic river floodplain: partitioning of phytoplankton, epipelon, macrophyte, and epiphyton production among lakes on the Mackenzie Delta *Ecosystems* **12** 853–72

Stanley E H and Del Giorgio P A 2018 Toward an integrative, whole network approach to C cycling of inland waters *Limnol. Oceanogr. Lett.* **3** 39–40

Sulla-Menashe D, Woodcock C E and Friedl M A 2018 Canadian boreal forest greening and browning trends: an analysis of biogeographic patterns and the relative roles of disturbance versus climate drivers *Environ. Res. Lett.* **13** 14007

Tank S E, Lesack L F W and Hesslein R H 2009 Northern delta lakes as summertime CO 2 absorbers within the arctic landscape *Ecosystems* **12** 144–57

Topp S N, Pavelsky T M, Jensen D, Simard M and Ross M R V 2020 Research trends in the use of remote sensing for inland water quality science: moving towards multidisciplinary applications' *Water* **12** 169

Tucker C J 1979 Red and photographic infrared linear combinations for monitoring vegetation *Remote Sens. Environ.* **8** 127–50

Vanhellemont Q 2019 Adaptation of the dark spectrum fitting atmospheric correction for aquatic applications of the Landsat and Sentinel-2 archives *Remote Sens. Environ.* **225** 175–92

Vermote E *et al* 2006 Second simulation of a satellite signal in the solar spectrum-vector (6SV) *6S User Guide* Version 3.2 pp 1–55 (https://www.researchgate.net/publication/247461276_Second_simulation_of_a_satellite_signal_in_the_solar_spectrum-vector_6SV)

Vermote E *et al* 2016 Preliminary analysis of the performance of the Landsat 8/OLI land surface reflectance product *Remote Sens. Environ.* **185** 46–56

Verpoorter C, Kutser T, Seekell D A and Tranvik L J 2014 A global inventory of lakes based on high-resolution satellite imagery *Geophys. Res. Lett.* **41** 6396–402

Vesterinen J, Devlin S P, Syväranta J and Jones R I 2016 Accounting for littoral primary production by periphyton shifts a highly humic boreal lake towards net autotrophy *Freshwater Biol.* **61** 265–76

Virtanen P *et al* 2020 SciPy 1.0: fundamental algorithms for scientific computing in Python *Nat. Methods* **17** 261–72

Vogelmann J E *et al* 2016 Perspectives on monitoring gradual change across the continuity of Landsat sensors using time-series data *Remote Sens. Environ.* **185** 258–70

Vonk J E *et al* 2015 Reviews and syntheses: effects of permafrost thaw on Arctic aquatic ecosystems *Biogeosciences* **12** 7129–67

Walvoord M A and Striegl R G 2007 Increased groundwater to stream discharge from permafrost thawing in the Yukon River basin: potential impacts on lateral export of carbon and nitrogen *Geophys. Res. Lett.* **34**

Walvoord M A, Voss C I and Wellman T P 2012 Influence of permafrost distribution on groundwater flow in the context of climate-driven permafrost thaw: example from Yukon Flats Basin, Alaska, United States *Water Resour. Res.* **48**

Wang C-K and Philpot W D 2007 Using airborne bathymetric lidar to detect bottom type variation in shallow waters *Remote Sens. Environ.* **106** 123–35

Wang J, Sheng Y and Tong T S D 2014 Monitoring decadal lake dynamics across the Yangtze Basin downstream of Three Gorges Dam *Remote Sens. Environ.* **152** 251–69

Wang J A, Sulla-Menashe D, Woodcock C E, Sonnentag O, Keeling R F and Friedl M A 2019 Extensive land cover change across Arctic-Boreal Northwestern North America from disturbance and climate forcing *Global Change Biol.* **26** 807–22

Wauthy M, Rautio M, Christoffersen K S, Forsström L, Laurion I, Mariash H L, Peura S and Vincent W F 2018 Increasing dominance of terrigenous organic matter in circumpolar freshwaters due to permafrost thaw *Limnol. Oceanogr. Lett.* **3** 186–98

Werdell P J *et al* 2019 The Plankton, Aerosol, Cloud, ocean Ecosystem mission: status, science, advances *Bull. Am. Meteorol. Soc.* **100** 1775–94

Wetzel R G 2001 *Limnology: Lake and River Ecosystems* (Cambridge, MA: Academic Press)

Wetzel R G and Hough R A 1972 Productivity and the Role of Aquatic Macrophytes in Lakes: An Assessment Productivity and the Role of Aquatic Macrophytes in Lakes: An Assessment *Technical Report No. COO-1599-54; CONF-720620-1* (Hickory Corners, MI: WK Kellogg Biological Station) (https://osti.gov/servlets/purl/4639975)

Wik M *et al* 2016 Climate-sensitive northern lakes and ponds are critical components of methane release *Nat. Geosci.* **9** 99–105

Yousef F, Charles Kerfoot W, Shuchman R and Fahnenstiel G 2014 Bio-optical properties and primary production of Lake Michigan: insights from 13-years of SeaWiFS imagery *J. Great Lakes Res.* **40** 317–24

Zhu Z, Wang S and Woodcock C E 2015 Improvement and expansion of the Fmask algorithm: cloud, cloud shadow, and snow detection for Landsats 4–7, 8, and Sentinel 2 images *Remote Sens. Environ.* **159** 269–77